

LARGE-EDDY SIMULATION OF A PSEUDO-SHOCK SYSTEM IN A LAVAL NOZZLE

J.F. Quatz, M. Giglmaier, S. Hickel, N.A. Adams

Institute of Aerodynamics and Fluid Mechanics
Technische Universität München

Boltzmannstraße 15, 85748 Garching b. München, Germany
quatz@tum.de

ABSTRACT

We present a high fidelity Large-Eddy Simulation (LES) of a pseudo-shock system in the divergent part of a Laval nozzle with rectangular cross section. The parallel side walls are taken into account, all wall boundary layers are well resolved and no wall model is used. For the first time it was possible to perform a wall-resolved LES for the same parameter set of a reference experiment. The results are validated against experimental wall-pressure measurements and schlieren pictures. Detailed insight into the complex 3-D flow phenomena including corner vortices and recirculation zones is presented. Differences between our LES and RANS simulations are discussed.

INTRODUCTION

Depending on the applied back pressure, transonic Laval nozzle flows can develop a compression shock that decelerates the flow from supersonic to subsonic speed. Inviscid theory predicts an instantaneous change of the flow variables through a single normal shock. Taking viscous effects into consideration, the boundary layers at the nozzle walls interact with the shock. A so-called pseudo-shock system develops, which is generally a sequence of several oblique shocks and expansion waves.

Pseudo-shock systems affect the performance and the reliability of processes and facilities in many fields of engineering, see Matsuo *et al.* (1999) for a comprehensive overview. Although there are several previous experimental and numerical studies, the mechanisms that govern the dynamic behavior of pseudo-shock systems are not yet sufficiently understood. Key mechanisms such as the interaction between three dimensional shocks and backflow regions cannot be analyzed and explained by experiments alone. Numerical simulations solving the compressible Reynolds-averaged Navier-Stokes (RANS) equations show a high sensitivity of the results to details of the applied turbulence model. In particular, two-equation eddy viscosity models give poor predictions of the mean flow. Results for Reynolds stress models that are based on the ω -formulation generally are in much better agreement with experimental data. However, RANS simulations cannot capture high-frequency unsteady processes. This motivates a high fidelity numerical investigation with a Large-Eddy Simulation (LES) resolving a much larger range of turbulent scales.

SETUP

Geometry of the flow channel as well as operating conditions of this numerical investigation are adapted to a comprehensive experimental study conducted by Gawehn *et al.* (2010) at DLR. The test rig is designed as double choked Laval nozzle system. The pseudo-shock system is located in the divergent part of the primary nozzle. In contrast to constant-area ducts (Carroll & Dutton, 1990; Morgan *et al.*, 2012, e.g.), in this experiment the shock position is well defined by the wall contour and the boundary conditions. Parallel side walls at the primary nozzle allow for schlieren imaging. The test rig is equipped with 47 pressure ports to record the wall pressure distribution. Assuming adiabatic operating conditions, shock position and pre-shock Mach number are defined by the ratio of the stagnation pressures p_{02}/p_{01} at the exit and the entry of the nozzle, which is a function of the quotient of the critical cross section areas A_1^*/A_2^* . In the experiment, the secondary critical cross section area A_2^* can be adjusted by a movable, slender cone to allow for different stagnation pressure ratios.

The investigated operation point is characterized by a stagnation pressure of $p_{01} = 4.8\text{bar}$ and a stagnation temperature of $T_0 = 300\text{K}$ at the inlet of the primary nozzle. The operating fluid is air. The stagnation pressure ratio is $p_{02}/p_{01} = 0.6$, which results in the shock position $x_s \approx 0.135\text{m}$ measured from the primary critical cross section A_1^* . These conditions correspond to a pre-shock Mach number of $M \approx 1.9$ and a Reynolds number of $Re_\delta \approx 10^5$ based on the boundary layer thickness δ , which extends to approx. 36% of the channel half height. A sketch of the apparatus and the flow conditions is given in fig. 1a), which shows the Mach number distribution at the symmetry slice $z = 0$.

The LES-solver INCA is applied for conducting the LES. The hyperbolic fluxes are discretized by the adaptive local deconvolution method ALDM (Hickel *et al.*, 2006; Hickel & Larsson, 2009). Build into this finite-volume discretization method is a subgrid-scale turbulence model that is consistent with turbulence theory. ALDM can capture shock waves while smooth waves and turbulence are propagated without excessive numerical dissipation. These features make ALDM applicable to the full Mach range of practical applications and particularly suitable for LES of shock-turbulence interactions as demonstrated also, e.g., by Grilli *et al.* (2012). Linear terms are discretized by second order centered differences and an explicit 3rd order Runge-Kutta method is used for time integration.

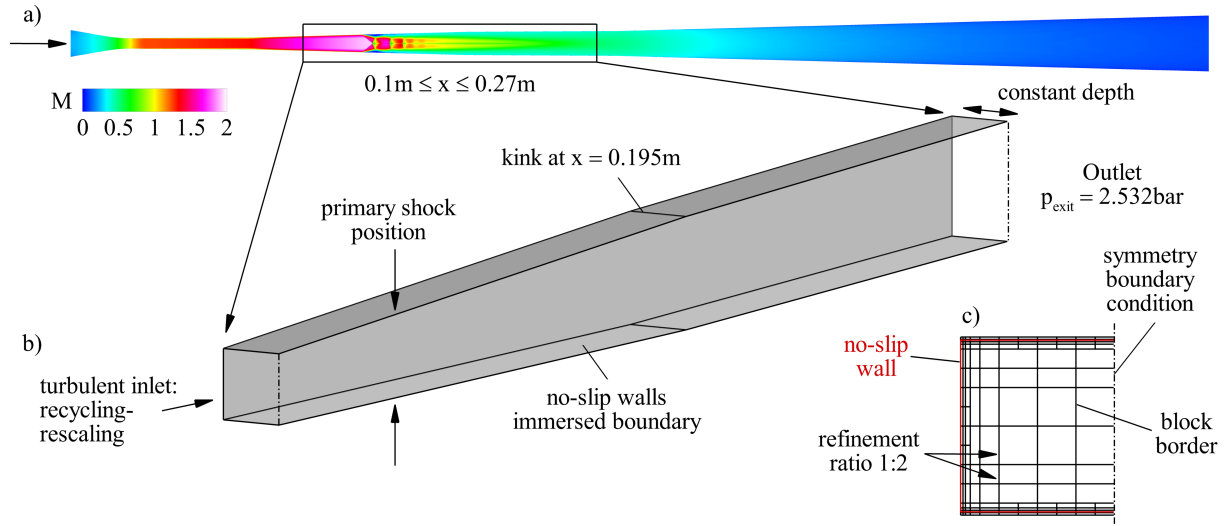


Figure 1: Overview of the LES setup.

- a Mach number distribution at the symmetry plane $z = 0$ within the primary Laval nozzle predicted by a RANS simulation with the BSL EARSM turbulence model applied. The secondary Laval nozzle is not shown. The black box indicates the LES domain.
- b Geometry and boundary conditions of the LES.
- c Sketch of the AMR block topology for the LES inlet plane.

In contrast to earlier work (Olson & Lele, 2011, e.g.), we simulate the full 3-D geometry of the rectangular nozzle duct including side walls. Hence, effects of secondary flow features, such as geometrically induced corner vortices and flow separation, are taken into account. To facilitate this extensive simulation, the computational domain is confined to the region of the flow channel ($0.1\text{m} \leq x \leq 0.27\text{m}$), where the pseudo-shock system is located. The LES sub-domain is marked by the box in fig. 1a). The non-parallel upper and lower walls consist each of two parts with the constant slope angles $\alpha_1 = 1.5^\circ$ and $\alpha_2 = 0.3^\circ$. The sections are connected by a sharp kink at $x = 0.195\text{m}$.

INCA solves the compressible Navier-Stokes equations on Cartesian multi-block grids. It also provides a built-in mesh generator enabling adaptive mesh refinement (AMR) for efficiently resolving the channel walls. The boundary layer refinement of the block topology normal to the mean flow direction x is illustrated in fig. 1c). The applied refinement ratio at block borders is set to 2. AMR also allows for the generation of high-quality initial conditions through grid sequencing, which strongly reduces the computational time necessary for reaching statistically stationary flow conditions. Due to the constant channel depth $\Delta z = 15 \cdot 10^{-3}\text{m}$, initial investigations with reduced computational effort are performed by applying a symmetry boundary condition at $z = 0$. The presented results are obtained on a grid of $190 \cdot 10^6$ cells in 8242 blocks. In the talk at the conference we will also present numerical results for the full channel.

To represent arbitrary geometries, INCA employs an immersed boundary method, which is used for the diverging upper and lower nozzle walls (see fig. 1b)). The parallel side walls at $z = \pm 7.5 \cdot 10^{-3}\text{m}$ are represented by a no-slip condition at the regular cell faces. Performance is improved by a linear stretching of the cells normal to the side wall. The boundary layer turbulence is resolved by the computational grid and no wall model is applied. The averaged dimensionless size of the wall cells is $\Delta y^+ \approx 2$. All walls

are assumed to be adiabatic, which is reasonable for steady-state flow conditions.

For generating physical turbulent inflow conditions, we use a recycling-rescaling method (Petrache *et al.*, 2011). Mean target values for the LES inlet ($x_i = 0.1\text{m}$) are extracted from a steady-state RANS simulation of one quarter of the whole flow channel. The RANS is performed with the commercial solver ANSYS CFX Release 14.0 and an explicit algebraic Reynolds stress model (EARSM - for details see Wallin & Johanson (2000)) featuring the BSL implementation (Hellsten, 2004). Gliglmaier *et al.* (2012) give a rationale for choosing this particular RANS turbulence model. To suppress spurious periodic disturbances, the recycled turbulence is mirrored at the symmetry plane of the test rig, $y = 0$. That is, the fluctuations occurring in the upper half of the channel are re-introduced into the lower part and vice versa. The recycling length is approximately nine times the boundary layer thickness.

A static pressure of $p_{\text{exit}} = 2.532\text{bar}$ is prescribed at the end of the shortened LES domain. This value is derived from measurements and RANS simulations.

The fluid is modeled as ideal gas with the material properties of air and Sutherland's law is used for viscosity and conductivity.

The explicit time integration method requires that the Courant-Friedrichs-Lewy stability criterion is fulfilled during the complete simulation, which results in an averaged time step size of $\Delta t \approx 3.4 \cdot 10^{-9}\text{s}$. The overall simulation (including grid sequencing) spans a physical time of $\approx 35 \cdot 10^{-3}\text{s}$. The statistical analysis of the LES data is based on a time period of 10^{-3}s . For reference, the flow through time of the confined LES domain is approx. $6 \cdot 10^{-4}\text{s}$ within the core flow region. The simulations are performed at the SuperMUC operated by the LRZ supercomputing center and consumed about $7 \cdot 10^6$ CPU-hours including the grid sequencing steps.

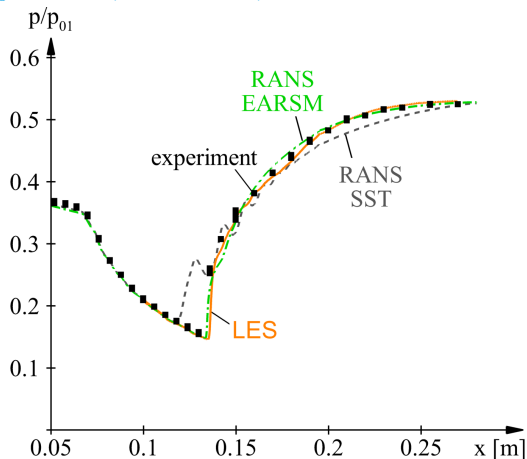


Figure 2: Normalized wall pressure distribution along the upper channel wall at the symmetry plane $z = 0$. The squares denote measurements by Gawehn *et al.* (2010), the dashed line the SST RANS results, the dash-dotted line results obtained by EARSM RANS simulation and the solid line the time averaged LES results.

RESULTS

Figure 2 shows the dimensionless pressure distribution along the upper channel wall. Supersonic flows within divergent nozzles are characterized by an acceleration accompanied by a decrease of the static pressure. The change back to subsonic conditions is managed by a pseudo-shock. The primary shock appears as an instantaneous pressure jump at the wall. Downstream, the supersonic regions within the pseudo-shock system are bent to the middle of the channel. Thus, the pressure footprint of the subsequent shock train is smeared out and results in a steady pressure rise at the wall. Proceeding further downstream, the flow is decelerated and further compressed. Besides measurements (symbols) and LES data (solid line), fig. 2 shows results for RANS simulations with Menter's SST model (Menter, 1994) and the EARSM (dashed and chain-dotted line). The SST model fails to predict correctly both the shock position and the mixing zone. The pressure footprint for the EARSM RANS simulation is, in general, in good agreement with the experiment. Nevertheless, some deviations are observed in the post-shock region. The LES data agree best with the pressure measured in the experiment. The LES results represent the supersonic flow in the pre-shock region very accurately and recover the experimental shock position exactly. Moreover, the measurement points directly downstream of the pressure jump are all well captured.

The validation of the LES against the experiment is continued in fig. 3 on the basis of schlieren pictures. Schlieren photographs can only provide integrated information about the density gradient. For this reason, a comparison between experiments and simulations is only meaningful if the numerical results are spatially averaged along the view direction. The schlieren pictures presented in fig. 3 show the axial density gradient $\partial\rho/\partial x$. Compressions are colored black and expansions occur bright.

The figures 3a) and 3b) are evaluated with schlieren imaging in z -direction through the parallel side walls. In agreement with Matsuo *et al.* (1999), the experiment shows a clearly developed bifurcated shape of the primary shock leading to a Mach reflection at the centerline. This is accurately reproduced by the LES but not correctly captured

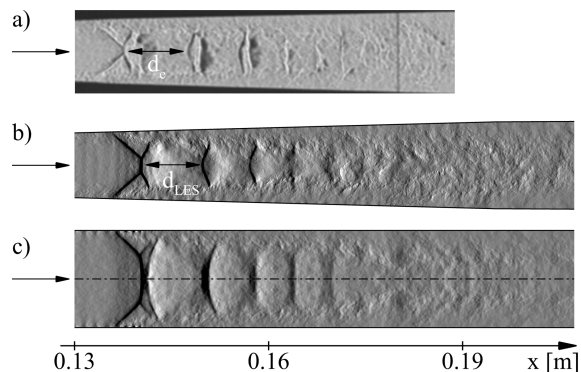


Figure 3: Schlieren pictures showing the axial density gradient $\partial\rho/\partial x$. Compressions appear black and expansions are white.

- a Experimental schlieren photography through the parallel side walls.
- b Transient snapshot of the LES spatially averaged along the z -direction.
- c Transient snapshot of the LES spatially averaged along the y -direction.

by the RANS simulations. Schlieren pictures for LES and experiment show that the primary shock is followed by four normal shocks. Also the distance between the subsequent shocks is reproduced very well with a deviation of only $(d_e - d_{LES})/d_e \approx 1\%$.

Note that experimental imperfections due to gaps at the glass-side-wall sealing, see Giglmaier *et al.* (2012), are responsible for the slightly shifted shock position seen in the schlieren pictures for experiment and the LES. The pressure signal shown in fig. 2 has been taken from another realization of the experiment with perfectly sealed metal side walls. The gap-free experiment shows a perfect agreement for the primary-shock location with the LES.

Figure 3c) shows a schlieren picture along the y -direction. This view is not available for the experiments due to the diverging channel geometry. It is obvious that the flow structure is inhomogeneous along the channel depth. The oblique part of the primary shock ranges over approximately half of the channel depth. For this reason, simulations that neglect the influences of the parallel side walls cannot provide reliable results for channels with rectangular cross sections with a low aspect ratio. Comparing both numerical schlieren pictures, we find that the onset of the oblique shock is located at the same coordinate x_s at the side walls and the diverging walls.

The highly resolved LES data allow for a detailed insight into the three dimensional structure of the entire pseudo-shock system. Figure 4 shows the complex shape of the $\langle M \rangle = 1$ iso-surface in yellow. The supersonic region at the symmetry plane is colored by the Mach number to distinguish super- and subsonic regions within the shock train in fig. 4a). The blue regions visualize the backflow zones in the domain by the slightly negative axial velocity $\langle u \rangle = -10^{-3} \text{m/s}$. Two major phenomena can be distinguished: First, the primary shock leads to flow separation and a recirculation zone that extends over the full channel depth at the diverging wall. In contrast, only very small backflow regions are found along the parallel side walls. Second, large corner separations develop along the channel edges downstream of the primary shock.

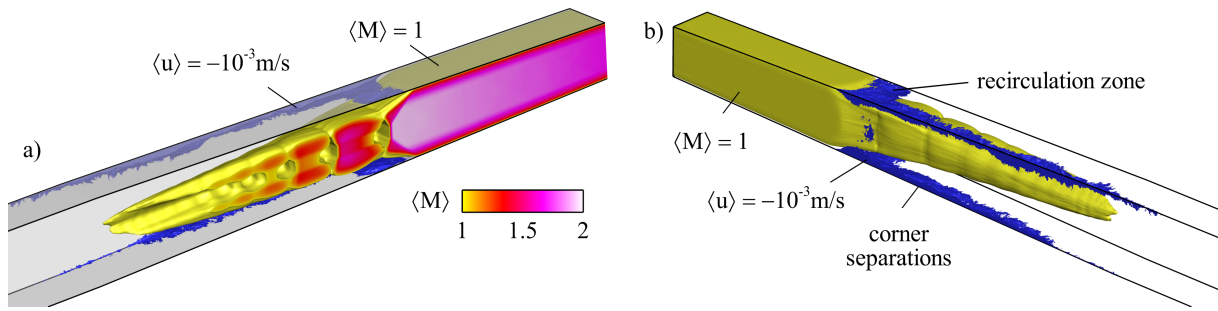


Figure 4: Mean 3-D structure of the pseudo-shock system. The yellow iso-surfaces correspond to $\langle M \rangle = 1$. The blue regions denote the axial velocity $\langle u \rangle = -10^{-3}$ m/s and indicate backflow regions.

- a View through the symmetry plane. Supersonic regions on the symmetry plane are colored with the local mean Mach number $\langle M \rangle$.
- b View from outside through the parallel side wall at $z = 7.5 \cdot 10^{-3}$ m.

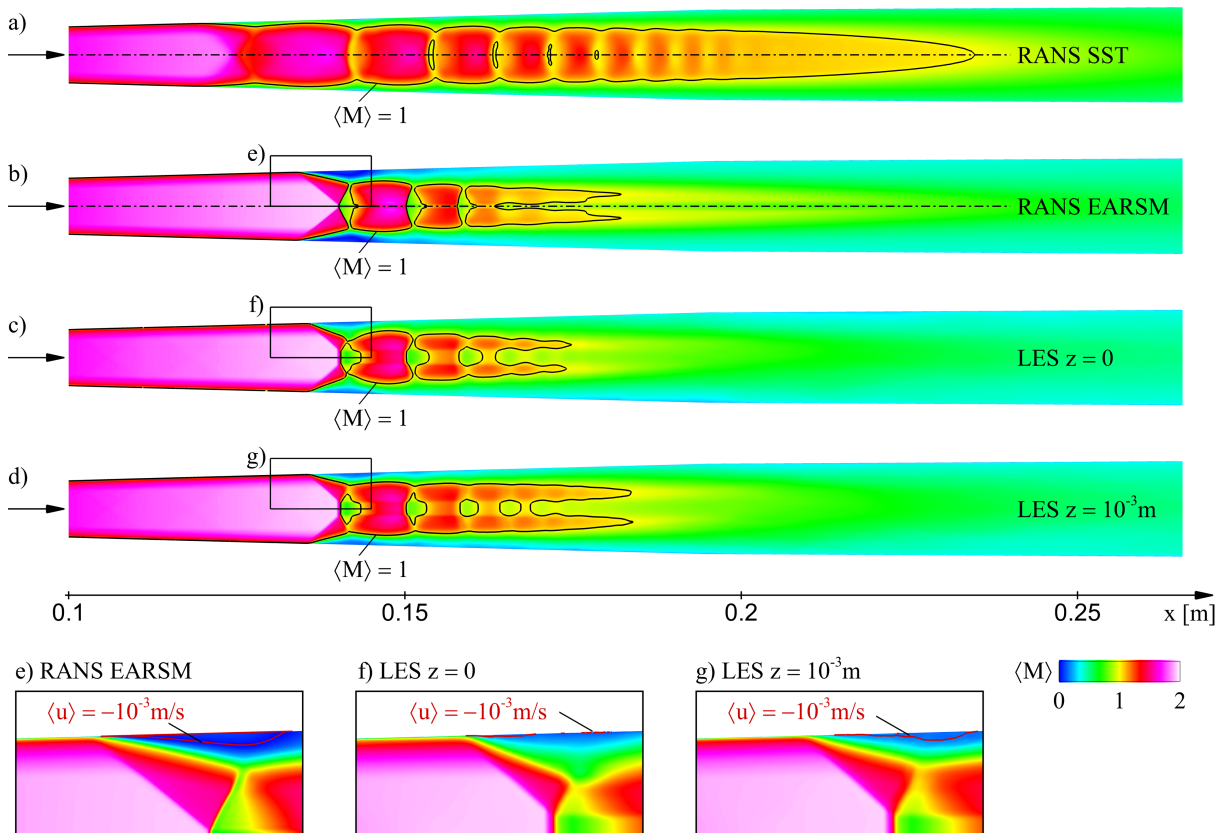


Figure 5: Mean Mach number distribution $\langle M \rangle$ on xy -slices. The black lines correspond to $\langle M \rangle = 1$. Red lines in the cutouts e-g indicate $\langle u \rangle = -10^{-3}$ m/s to visualize the recirculation zones. The RANS results are mirrored at the centerline of the channel (dash-dotted). Unless otherwise noted, the symmetry slice $z = 0$ is shown.

- a SST RANS simulation.
- b EARSM RANS simulation.
- c ALDM LES.
- d ALDM LES at slice $z = 10^{-3}$ m.
- e-g Cutout of figures b)-d). The locations and dimensions are marked by black boxes in the corresponding pictures above.

In the following we compare results obtained by RANS simulations with the statistical mean flow data of the LES. Figure 5 shows the time averaged Mach number distributions $\langle M \rangle$ at the symmetry plane $z = 0$ for the RANS approach with the SST (5a) and the EARSM (5b) turbulence

model applied, and the LES (5c). Results for the EARSM are in reasonable agreement with LES data. The mean shock train consists of four distinguishable single shocks. Due to shock motion, this number might differ in instantaneous snapshots, such as in the schlieren pictures in fig. 3. Further

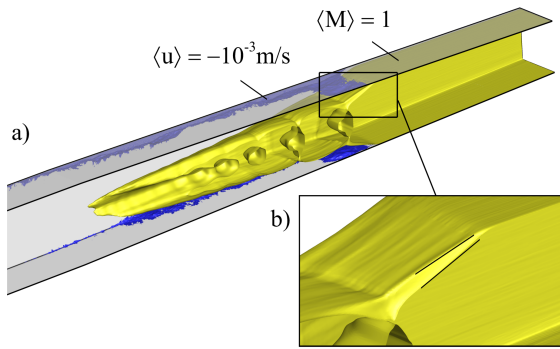


Figure 6: Time averaged 3-D structure of the pseudo-shock system. Yellow iso-surfaces correspond to $\langle M \rangle = 1$ and blue regions indicate backflow with the axial velocity $\langle u \rangle = -10^{-3} \text{m/s}$. The direction of view is aligned through the symmetry plane $z = 0$ and the channel geometry is included. The cutout b) gives detailed insight into irregularities of the flow structure near the symmetry boundary condition. The two black lines illustrate the change of the shock angle.

downstream, the shock-free compression within the mixing region is also well represented by the EARSM RANS. The overall shape and length of the pseudo-shock system is similar for EARSM RANS and LES.

The comparison of SST and EARSM results shows the sensitivity of the RANS simulation with respect to the applied turbulence model. The simulation with SST model shown in fig. 5a) fails to predict position, length and structure of the shock train.

In spite of the overall agreement of fig. 5b) and 5c), differences can be found in the details. In contrast to LES and experiment, the EARSM RANS solution does not exhibit a Mach reflection at the centerline of the channel. The black line corresponding to $\langle M \rangle = 1$ shows an obvious deviation of the primary oblique shock angle, which is steeper for the LES.

In the cutouts 5e) and 5g) the recirculation zones are visualized by red lines, which indicate a slightly negative value of the axial velocity $\langle u \rangle$. While the RANS solution shows a distinct backflow region, which interacts with the primary shock, the LES mean values do not show significant reverse flow. Analyzing a parallel xy -slide nearby (fig. 5d) and g) reveals that the absence of the recirculation zones is a local phenomenon at the symmetry boundary condition of the LES. Moreover, the shock angle of the pseudo-shock system predicted at $z = 10^{-3} \text{m}$ agrees slightly better with the EARSM RANS simulation. The sonic line downstream of the primary shock has a less baggy shape than at the symmetry plane and is in good agreement with the EARSM RANS result in fig. 5b). The major remaining difference between LES and EARSM RANS is the size of the normal-shock region at the centerline. The comparison with the experiment confirms the LES prediction, see fig. 3.

The effect of the symmetry boundary condition on the 3-D shape of the pseudo-shock system can be also observed in the cutout in fig. 6. Directly at $z = 0$, the $\langle M \rangle = 1$ iso-surface exhibits an unphysical kink, which extends throughout the entire shock train.

Contrary to RANS simulations, symmetry boundary conditions applied to LES suppress the velocity fluctuations normal to the boundary. Turbulent structures and vortices

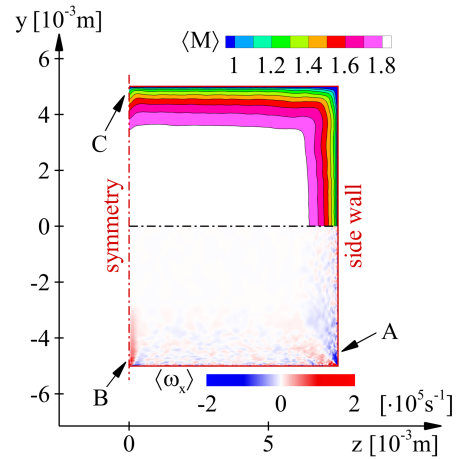


Figure 7: Time averaged Mach number (upper section) and axial vorticity component $\langle \omega_x \rangle$ (lower section) on a yz -slice through the LES domain located directly upstream of the primary shock at $x = 0.13 \text{m}$. The corner vortices due to the side wall (A), the small vortices at the symmetry boundary condition (B) and the resulting reduction of the Mach number (C) are accentuated.

can be affected. In the present case, this effect leads to the development of spurious corner vortices at the symmetry plane $z = 0$. These unphysical corner vortices are visualized and marked as (B) in the lower half of fig. 7, which is clearly shown by the sign change of the axial vorticity component $\langle \omega_x \rangle$. Although their intensity is very small compared to the physical vortices at the channel corners (A), their influence on the subsequent flow structures is not negligible. As consequence, the Mach number is reduced in the region of the vortices (C) and the shock angle is increased as already observed in fig. 5. In the inner domain the separated backflow is properly represented by the LES as shown by the blue regions in fig. 4. The observed problem can be avoided only by simulating the full channel geometry without applying a symmetry boundary condition. Such simulations of the full channel are currently in progress and results will be presented at the conference.

Figure 8 shows contour plots of the turbulence kinetic energy $k = \frac{1}{2} (\langle u'u' \rangle + \langle v'v' \rangle + \langle w'w' \rangle)$ for LES and RANS simulations. The distribution and the range of k predicted by the EARSM RANS and the LES are in good agreement. The shock motion resolved by the LES accounts for the higher values of k within the shock train. By definition, this cannot be reproduced by the RANS simulations. The SST model (fig. 8a) is not able to correctly represent structure and intensity of the turbulent flow features.

CONCLUSIONS AND OUTLOOK

In summary, the LES is able to predict the complex flow within the pseudo-shock system reliably and accurately. The results reproduce wall pressure measurements and experimental schlieren photographs very well. It is shown that it is crucially necessary to take the side walls into account and to avoid symmetry boundary conditions. This LES also enables for the first time a detailed validation of RANS turbulence models for pseudo-shock systems in turbulent duct flows. To this end, we can confirm the conclusions of the turbulence-model study by Giglmaier *et al.* (2012). In particular, two equation eddy viscosity models

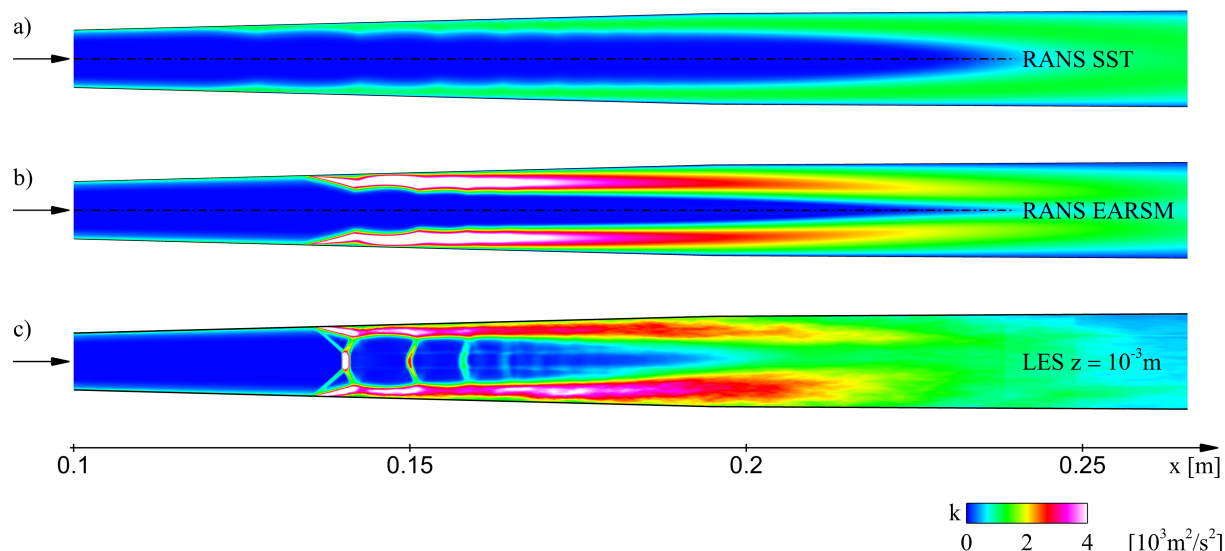


Figure 8: Turbulence kinetic energy k on xy -slices. The RANS results are mirrored at the centerline of the channel (dash-dotted). Unless otherwise noted, the symmetry slice $z = 0$ is shown.

- a) SST RANS simulation.
- b) EARSM RANS simulation.
- c) ALDM LES at slice $z = 10^{-3}$ m.

within this study represented by the SST model give poor predictions of the mean flow. Results for Reynolds stress models that are based on the ω -formulation generally are in much better agreement with experimental data.

ACKNOWLEDGMENTS

Computing resources for the presented work are provided by the Leibniz Rechenzentrum LRZ under grant PR45TU. The fruitful collaboration with Dr. Thomas Gawehn from the Institute of Aerodynamics and Flow Technology at the German Aerospace Center DLR is gratefully acknowledged.

REFERENCES

Carroll, B. F. & Dutton, J. C. 1990 Characteristics of multiple shock wave/turbulent boundary-layer interactions in rectangular ducts. *Journal of Propulsion and Power* **6** (2), 186–193.

Gawehn, T., Gülhan, A., Giglmaier, M., Al-Hasan, N. S., Quaatz, J. F. & Adams, N. A. 2010 Analysis of pseudo-shock system structure and asymmetry in laval nozzles with parallel side walls. In *19th International Shock Interaction Symposium*. Moscow, Russia.

Giglmaier, M., Quaatz, J. F., Gawehn, T., Gülhan, A. & Adams, N. A. 2012 Numerical and experimental investigations of pseudo-shock systems in a planar nozzle - impact of bypass mass flow due to narrow gaps (accepted). *Shock Waves*.

Grilli, M., Schmid, P. J., Hickel, S. & Adams, N. A. 2012 Analysis of unsteady behaviour in shockwave turbulent

boundary layer interaction. *Journal of Fluid Mechanics* **700**, 16–28.

Hellsten, A. 2004 New advanced k - ω turbulence model for high-lift aerodynamics. *AIAA Paper* (2004-1120).

Hickel, S., Adams, N. A. & Domaradzki, J. A. 2006 An adaptive local deconvolution method for implicit les. *Journal of Computational Physics* **213** (1), 413 – 436.

Hickel, Stefan & Larsson, Johan 2009 On implicit turbulence modeling for les of compressible flows. In *Advances in Turbulence XII* (ed. Bruno Eckhardt), *Springer Proceedings in Physics*, vol. 132, pp. 873–875. Springer Berlin Heidelberg.

Matsuo, K., Miyazato, Y. & Kim, H.-D. 1999 Shock train and pseudo-shock phenomena in internal gas flows. *Progress in Aerospace Sciences* **35** (1), 33 – 100.

Menter, F. R. 1994 Two-equation eddy-viscosity turbulence models for engineering applications. *AIAA Journal* **32** (8), 1598 – 1605.

Morgan, B., K., Duraisamy & Lele, S. K. 2012 Large-eddy and rans simulations of a normal shock train in a constant-area isolator. *AIAA Paper* (2012-1094).

Olson, B. J. & Lele, S. K. 2011 Large-eddy simulation of an over-expanded planar nozzle. *AIAA Paper* (2011-3908).

Petrache, O., Hickel, S. & Adams, N. A. 2011 Large eddy simulations of turbulent enhancement due to forced shock motion in shock-boundary layer interaction. *AIAA Paper* (2011-2216).

Wallin, S. & Johanson, A. V. 2000 An explicit algebraic reynolds stress model for incompressible and compressible turbulent flows. *Journal of Fluid Mechanics* **403**, 89–132.